biology

MDPI

Article

Multi-Omics Analysis of Radiation-Induced Heart Disease and Validation of PHLDA3 Expression

Gang Wang [1], Yang Zhong [2], Ai-Jun Wei [1] and Ping Xie [1,2,*]

[1] The First School of Clinical Medicine, Lanzhou University, Lanzhou 730000, China; wg502592901wg@163.com (G.W.); waj112203@163.com (A.-J.W.)
[2] The First Clinical Medical College, Gansu University of Chinese Medicine, Lanzhou 730000, China; 18294183137@163.com
* Correspondence: pingx189@outlook.com

Simple Summary

Radiotherapy for chest tumors can damage the heart, but the molecular changes involved are still not fully understood. In this study, we analyzed changes in the mouse heart after irradiation at three levels: chemical marks on the genetic material, gene expression, and protein levels, and screened for candidate molecules for further study. By cross-comparing the results across these layers, we identified a protein called PHLDA3 as the priority candidate for further study. In a separate group of mice, staining for PHLDA3 was stronger in heart tissue after irradiation. The overall analysis also identified molecular changes related to cellular energy supply and to remodeling of tissue structure. These findings help characterize the molecular features of radiation-induced heart injury and provide leads for exploring strategies to protect the heart. Whether PHLDA3 is directly involved in the injury and whether altering its expression can produce a protective effect still requires further experimental testing.

Abstract

Radiation-induced heart disease (RIHD) is a serious adverse effect of tumor radiotherapy, with no effective treatment or key target. We integrated DNA methylation, transcriptomic, and proteomic data from mouse myocardium collected 12 weeks after cardiac irradiation in a mouse model of RIHD to characterize radiation-associated molecular alterations and prioritize candidate genes. Myocardial injury in mice was assessed by H&E staining, transmission electron microscopy, and serum BNP measurements. Injury in irradiated H9c2 cells was assessed by cell viability and LDH release. Candidates were screened by cross-layer direction, three-layer overlap, co-expression networks, and differential, pathway, and sensitivity analyses. Irradiation caused myocardial histological and ultrastructural damage and raised serum BNP; in H9c2 cells, viability fell and LDH release rose. PHLDA3 was the only gene overlapping all three omics layers. Both RNA and protein were upregulated, with FDR support for the proteome model (FDR = 0.0358) but not for RNA (0.0713). In GSE255063, which also contributed to the co-expression network, *Phlda3* expression was higher in irradiated mice at both 1 day and 6 weeks, with statistical support only at 1 day. Immunohistochemistry in an independent group of mice showed stronger myocardial PHLDA3 staining after irradiation. Pathway analyses showed negative enrichment of mitochondrial gene sets, positive enrichment of extracellular matrix organization gene sets, and an increase in the inferred TGFβ transcriptional response score. Three-layer integration prioritized PHLDA3 for further study in radiation-induced myocardial injury. Its functional role remains to be established.

Check for updates

Academic Editor: Lei Ye

Received: 8 November 2026
Revised: 23 November 2026
Accepted: 24 November 2026
Published: 26 November 2026

Copyright: © 2026 by the authors. Licensee MDPI, Basel, Switzerland. This article is an open access article distributed under the terms and conditions of the Creative Commons Attribution (CC BY) license.

Keywords: radiation-induced heart disease; DNA methylation; transcriptome; proteome; PHLDA3

1. Introduction

Thoracic radiotherapy improves tumor control while exposing the cardiovascular system to radiation, which can lead to radiation-induced heart disease (RIHD) [1–3]. RIHD presents as inflammatory responses, microvascular abnormalities, myocardial remodeling, and fibrosis [4], and affects patients' cardiovascular outcomes over the long term after treatment [5]. At present, no effective treatment or defined therapeutic target is available for RIHD in clinical practice.

DNA methylation, RNA expression, and protein abundance reflect molecular changes at different levels. The relationship between DNA methylation and transcription depends on the position of the modified region [6] and on sequence context, and the direction of change in RNA does not necessarily coincide with the corresponding change in protein [7–9]. Comparing the direction of change across molecular layers, the molecules shared between layers, and the common biological processes, and then testing expression in tissue, therefore helps to assess how consistent the supporting evidence for a given candidate molecule is. Our previous study characterized transcriptomic and proteomic changes in irradiated mouse myocardium and examined the role of DNMT1 in myocardial injury [10]. Park et al. reported that low-dose ionizing radiation altered DNA methylation patterns in human vascular endothelial cells [11]. In the present study, we asked whether incorporating myocardial DNA methylation data could narrow the previously reported RNA-protein candidate set and identify a candidate for protein expression assessment in an independent cohort of mice.

We integrated WGBS, RNA-seq, and proteome data from mouse myocardium 12 weeks after local cardiac irradiation, compared the direction of change in the DNA methylation-RNA and RNA-protein pairs, and screened for candidate molecules using three-layer overlap analysis and co-expression networks. Differential and pathway analyses in the full expression background, transcriptional response inference, and sample-sensitivity analyses served to describe the molecular response of the irradiated myocardium and to assess the stability of the candidate expression results. We used GSE255063, which also contributed to co-expression network construction, to check the direction of *Phlda3* expression changes and assessed myocardial PHLDA3 protein expression by immunohistochemistry in an independent cohort of mice.

2. Materials and Methods

2.1. Animal Model and Sample Collection

Male C57BL/6 mice aged 6–8 weeks were obtained from the Experimental Animal Center of the Lanzhou Veterinary Research Institute. Mice were housed at 24–26 °C and 40–60% relative humidity on a 12 h light/12 h dark cycle with food and water available ad libitum, and were acclimatized for 1 week before model establishment. Separate cohorts were used for the omics analyses and independent validation. Within each cohort, mice were randomly assigned to a control group (Ctrl) or an irradiation group (Radiation), with 10 mice initially allocated to each group. Mice were anesthetized by intraperitoneal injection of 1% pentobarbital sodium. The point of maximal apical impulse on the chest wall was identified as the positioning landmark. Each mouse was placed beneath a 10-cm-thick lead block mounted on a stand. The block had three circular apertures, each 1 cm in diameter. The apical impulse was aligned with the corresponding aperture, and the mouse was im-

mobilized in that position. Using a small-animal X-ray irradiator (Model No. 225, Precision X-ray Inc., Madison, CT, USA), the beam was directed vertically downward through the apertures toward the cardiac region. The irradiator operated at 225 kV and 13.3 mA, with a source-to-skin distance of 48 cm. A single nominal dose of 20 Gy was prescribed at an instrument dose rate of 2 Gy/min. Control mice underwent the same procedure without irradiation. The dose-rate reference position, the absorbed dose to the heart, and the extent of cardiac coverage could not be verified from the available records. Myocardial tissue and blood were collected at the scheduled 12-week endpoint. During follow-up, two irradiated mice in the omics cohort and three irradiated mice in the independent validation cohort died before scheduled sample collection. The causes of death were undetermined. These five mice were not included in any endpoint analysis.

WGBS and RNA-seq were performed on myocardial samples from the same three mice per group. The proteomic analysis included these mice and one additional mouse per group, giving four mice per group. The paired three-layer analysis used the six mice with data from all three layers, and the main proteomic analysis used all eight mice with proteomic data. For each non-omics in vivo endpoint, including blood measurements and immunohistochemistry, six mice per group were analyzed. Of the seven irradiated mice in the independent validation cohort that survived to the scheduled 12-week endpoint, samples from six mice were randomly selected for endpoint measurements. The intact heart and blood samples from the seventh mouse were stored at −80 °C as backup in case any selected sample was lost or damaged. These backup samples were not used in the reported analyses. No study-specific humane endpoint criteria were predefined. Following euthanasia at the scheduled endpoint, carcasses were disposed of by animal facility staff.

2.2. In Vivo Damage Markers and Relative PHLDA3 Expression

Serum brain natriuretic peptide (BNP) measurement: Blood was collected by retro-orbital puncture, left at room temperature for 1 h, and then centrifuged, and the upper serum layer was collected. BNP was measured with an ELISA kit (CEA541Mu, Cloud-Clone Corp., Wuhan, China). Standard, sample, and blank wells each received 50 µL of the corresponding solution followed by 50 µL of detection reagent A, and plates were incubated at 37 °C for 1 h and washed three times. Each well then received 100 µL of detection reagent B, was incubated at 37 °C for 30 min, and was washed three more times. After addition of 90 µL of substrate solution and color development at 37 °C in the dark, 50 µL of stop solution was added. Absorbance at 450 nm was measured on a microplate reader, and serum BNP concentrations were calculated from the standard curve.

H&E staining: Myocardial tissue was fixed in 4% paraformaldehyde, dehydrated through graded ethanol, cleared in xylene, embedded in paraffin, and sectioned. Sections were stained with hematoxylin, differentiated, blued, and counterstained with 0.5% eosin, then dehydrated, cleared, and mounted in neutral gum before being observed and photographed under a light microscope to assess myocardial fiber arrangement and nuclear morphology.

Immunohistochemistry (IHC): Myocardial tissue sections were incubated with 3% hydrogen peroxide at room temperature for 10 min and blocked with 5% BSA at room temperature for 30 min, then incubated with PHLDA3 primary antibody (#4294, Cell Signaling Technology, Danvers, Massachusetts, USA) overnight at 4 °C. An HRP-conjugated secondary antibody was added and incubated for 30 min at room temperature; after washing in PBS, DAB was applied for 3 min. After counterstaining with hematoxylin, bluing, dehydration, clearing, and mounting, sections were observed and photographed under a light microscope, and PHLDA3 protein expression was evaluated on the basis of the brown signal. PHLDA3 immunostaining was quantified in six mice per group. One microscopic

field from one myocardial section was analyzed per mouse. Images were analyzed in ImageJ 1.53a using the IHC Toolbox plugin. The analyst was aware of group assignments during image analysis. Each mouse contributed one measurement and served as the experimental unit for the between-group comparison.

2.3. Cell Culture and Model Establishment

The H9c2 cell line was purchased from the China Center for Type Culture Collection (CCTCC), Chinese Academy of Sciences. Cells were maintained in DMEM (Shanghai Yuanpei Biotechnology Co., Ltd., Shanghai, China) supplemented with 10% fetal bovine serum (ABWbio, Uruguay) and 1% penicillin–streptomycin 1% double antibiotics (100 U/mL penicillin +100 μg/mL streptomycin, Shanghai Yuanpei Biotechnology Co., Ltd., Shanghai, China). The culture conditions were 37 °C, 5% CO_2, and 95% air, with medium replaced every 2–3 days. Cells at approximately 80% confluence were used for experiments, with a control group and radiation groups receiving 4, 8, and 12 Gy. The 8 Gy dose was selected based on our previously published H9c2 irradiation model [10]. Doses of 4 and Gy were included to assess cell viability and LDH release at 48 h at doses below and above 8 Gy. Cells were irradiated with a small-animal irradiator, the medium was replaced immediately after irradiation, and the assays were carried out after a further 48 h of culture.

2.4. In Vitro Assessment of Radiation-Induced Cell Injury

Cell viability assay: H9c2 cells were seeded at 5000 cells per well in 96-well plates, cultured for 24 h, irradiated to establish the model, and then cultured for a further 48 h. CCK-8 reagent (cat. m4839, Abmole, Houston, TX, USA) was added at 10 μL per well, and after 2 h of incubation, absorbance at 450 nm was read on a microplate reader to assess relative cell viability. The CCK-8 assay was performed in at least three independent experiments, with six replicate wells per group in each experiment.

LDH release assay: At 48 h after irradiation, the culture supernatant was collected and assayed according to the instructions of the LDH detection kit (cat. A020-2-2, Nanjing Jiancheng Bioengineering Institute, Nanjing, China). Absorbance at 450 nm was measured on a microplate reader to determine the LDH level in the supernatant. The LDH assay was performed in at least three independent experiments, with three replicate wells per group in each experiment.

2.5. Transmission Electron Microscopy

Immediately after removal, myocardial tissue was placed in electron microscopy fixative and kept in the dark. Samples were treated with 1% osmium tetroxide containing 0.1% potassium ferrocyanide, processed with graded ethanol, acetone, and embedding medium, left overnight at 37 °C, and polymerized at 60 °C for 48 h. Ultrathin sections were prepared, stained with 2% ethanolic uranyl acetate and lead citrate for 15 min, left overnight at room temperature, and then imaged with a transmission electron microscope (Talos F200C, 200 kV, FEI, Hillsborough, OR, USA).

2.6. Omics Data Acquisition and Preprocessing

The present study reuses the mouse myocardial RNA-seq and proteome data from a previous study and additionally includes myocardial whole-genome bisulfite sequencing (WGBS) data that were not reported in that paper. The WGBS and RNA-seq data came from the same six mice, and these six mice were also included in the proteome analysis. The correspondence of samples across the omics datasets is given in Section 2.1 [10]. For whole-genome bisulfite sequencing (WGBS), libraries were prepared by DNA fragmentation, adapter ligation, and bisulfite treatment, and sequenced paired-end at 150 bp on an Illumina

NovaSeq 6000, with lambda DNA added to monitor conversion efficiency. Reads were quality-trimmed with Trimmomatic [12] and aligned to the mouse mm10 reference genome with BSMAP [13]. Gene identifiers were harmonized across omics layers for the intended analysis, and duplicate records were handled.

2.7. Differential Methylation and Differential Expression Analyses

Differentially methylated sites were analyzed with methylKit [14] with a minimum coverage of 10; sites were selected at $p < 0.01$ and |methylation difference| ≥ 0.1, and sites with $q < 0.05$ were flagged separately. Differentially methylated regions were called with metilene [15], with final criteria of pMWU < 0.05, |methylation difference| ≥ 0.1, at least 5 CpG sites, and region length ≥ 50 bp. Methylation differences were defined throughout as radiation minus control.

In the full-background reanalysis, RNA genes with at least 3 samples having counts ≥ 10 were retained and compared between groups with DESeq2 Wald tests. Duplicate protein records were collapsed to the mean log-scale expression per gene, and the protein data were analyzed with limma using the robust empirical Bayes approach. The main proteome analysis used all eight samples, and the six shared animals were used for subset sensitivity analysis; model specifications and identifier handling are described in Supplementary Methods S1.

2.8. Weighted Gene Co-Expression Network Analysis

Our RNA-seq data and the external dataset GSE255063 [16] were converted to TPM and merged at the level of shared Ensembl genes. After $\log2(\mathrm{TPM} + 1)$ transformation and ComBat correction for data source [17], a WGCNA network was constructed [18]. The network type was signed hybrid, the soft threshold was 20, the minimum module size was 30, and the module merging threshold was 0.25.

Module eigengenes were correlated with the radiation group and with data source, module tests for the radiation group were Bonferroni-corrected, and gene significance and module membership were computed for use in the subsequent candidate ranking. GSE255063 entered the network construction as extended data for the discovery stage; details are given in Supplementary Methods S2.

2.9. Cross-Omics Integration and Candidate Molecule Screening

DNA methylation and RNA results were linked through region–gene annotation, and the direction of change was compared between the two layers; where one gene corresponded to several regions, the record for each region was retained together with the heterogeneity in direction. RNA and protein were matched by unique gene, and the positive association between the directions of change was assessed with a one-sided Fisher exact test, with a binomial test as a supporting analysis.

Screening for candidate molecules prioritized three-layer overlap across DNA methylation, RNA, and protein, and candidates were ranked by combining cross-layer evidence with the WGCNA network scores. The candidate list was locked before the subsequent expression checks and experimental validation; the scoring rules are given in Supplementary Methods S3.

Sample-level integration of the three omics layers used DIABLO [19], restricted to the six fully matched animals with two components. This analysis was used to describe cross-omics latent variable relationships and feature loadings within the training samples; it did not contribute to candidate ranking or to the evaluation of classification performance.

2.10. Functional and Pathway Enrichment Analysis

For the discovery-stage RNA pathway analysis, genes with at least 3 samples having TPM ≥ 1 were retained, and log2 changes were computed from the ratio of group means after adding a pseudocount of 0.1 and used for ranking. For protein over-representation analysis, genes with $p < 0.05$ and $|\log2FC| > 0.5$ served as the foreground, and all genes corresponding to quantifiable proteins served as the background. Mouse GO, KEGG, and Reactome annotations were used [20–22]; BH correction was applied within each layer, and cross-layer results were compared by stable pathway ID, with a pathway reaching FDR < 0.05 in both layers defined as a two-layer consensus. ssGSEA scores were additionally computed for GO gene sets [23,24], and group differences were compared with Welch *t* test.

In the full-background analysis, preranked GSEA was performed with the RNA Wald statistic and the protein moderated t statistic, respectively [25], and CAMERA was used to assess the influence of inter-gene correlation within pathways on the results [26]. FDR was controlled within the complete test family of each analysis, and FDR < 0.05 was used to declare significant enrichment, with the full set of leading-edge members retained. Gene set scope and correlation parameters are given in Supplementary Methods S4.

2.11. Transcriptional Response and Transcription Factor Activity Inference

RNA counts were TMM-normalized [27], converted to logCPM, and centered gene by gene before being used for transcriptional response inference. A mouse-adapted PROGENy model was applied to infer pathway responses through a multivariate linear model [28], and the CollecTRI regulatory network was used to infer transcription factor activities through a univariate linear model, with at least 5 usable target genes per factor [29]. Pathway and factor scores were computed with decoupleR [30].

Animal-level scores were compared between groups with limma and BH-corrected within their respective complete test families. These scores reflect activities inferred from the expression data; prior networks and model parameters are given in Supplementary Methods S5.

2.12. Candidate Gene Expression Analysis in a Public Dataset

After the candidate molecules had been defined, a targeted expression check of Phlda3 was performed using the raw counts in GSE255063 [16]. Samples at 1 day and 6 weeks after irradiation in GSE255063 were modeled separately with DESeq2, comparing the radiation group with the control group and reporting normalized counts, log2 fold change, Wald test *p* value, and BH-FDR over the full gene background.

Because this dataset had already contributed to the WGCNA network, the analysis was used to check the direction of candidate gene expression and was not treated as independent external validation of the discovery workflow, nor was the candidate ranking revised on the basis of it. Sample grouping and gene mapping are given in Supplementary Methods S6.

2.13. Robustness and Sensitivity Analyses

Result stability was assessed by comparing the eight-sample and six-sample protein models and by varying inference parameters. Leave-one-out analyses of RNA and protein expression refitted the differential model after each animal was removed; leave-one-out analyses of pathway and transcription factor scores retained the existing normalization and scores and compared only the direction of the group mean in the remaining animals.

In addition, the inferred scores were recomputed after Phlda3 was removed from the expression input and from the target genes of the prior networks, to assess how dependent the results were on that gene. The full-sample model was always taken as the main result,

and multiple-testing correction was applied separately to each sensitivity version; details are given in Supplementary Methods S7.

2.14. Transcriptome-Proteome Expression Association Analysis

Only the six shared animals were used, and RNA and protein expression were matched by unique Entrez ID. Overall RNA–protein associations were assessed using Spearman correlation. For the group-adjusted analysis, RNA and protein expression values were separately converted to average ranks across the six animals. Each set of ranks was regressed on group, and Pearson correlation was calculated between the two sets of residuals.

The overall test enumerated all 720 pairings and the group-conditioned test enumerated all 36 within-group pairings, using two-sided exact permutation tests, with BH correction applied separately over all analyzable genes. Phlda3 was additionally examined in a descriptive leave-one-out analysis. Individual-level correlation with RNA could not be computed for the target methylation regions because per-animal values were not available. Permutation and leave-one-out rules are given in Supplementary Methods S8.

2.15. Statistical Analysis

Quantitative experimental data are expressed as mean ± SD. Two-group comparisons used *t* tests, and one-way analysis of variance (ANOVA) was used for comparisons among multiple groups. Parametric tests were used because the experimental outcomes were continuous and the comparisons of interest were differences in group means. No formal tests of residual normality or, where applicable, homogeneity of variance were performed. Given the small number of independent observations, departures from these assumptions could affect the reported *p* values, and the results should be interpreted with this limitation in mind. Statistical analysis and plotting of experimental data were performed in GraphPad Prism 9.5, and cell experiments were repeated independently at least three times. Statistical analysis and visualization of the omics data were carried out mainly in R 4.6.1; data table parsing, verification of coordinates and thresholds, and consistency testing were performed in Python 3.13.7. Where multiple testing was involved, statistical support was judged on the basis of the q value, the BH-FDR, or the Bonferroni-corrected result as pre-specified for the analysis concerned.

3. Results

3.1. X-Ray Irradiation Induces Damage to Myocardial Tissue and Cells

The previous study characterized the damage phenotype after irradiation by H&E staining, transmission electron microscopy, serum BNP measurement, and CCK-8 and LDH assays in H9c2 cells. Figure 1A–C of the present study come from animal samples from batches different from those used in the previous study, and Figure 1D–E come from independently performed H9c2 experiments; the images and measurement data shown were generated in the present experiments. H&E staining indicated more orderly myocardial fiber arrangement and intact nuclear morphology in the control group; in the radiation group, some myocardial nuclei had dissolved, and no obvious inflammatory cell infiltration was observed (Figure 1A). TEM showed orderly myofibrillar alignment with distinct Z lines and M lines, intact mitochondrial morphology and double-membrane structure, and well-preserved continuity of the mitochondrial cristae in the control group; in the radiation group, myofibrillar alignment was disrupted, the Z and M lines were blurred, and the double-membrane structure of some mitochondria was indistinct with cristae continuity damaged (Figure 1B). The H&E and TEM findings were descriptive. We did not quantify myocardial fibrosis, tissue remodeling, or the extent of ultrastructural abnormalities.

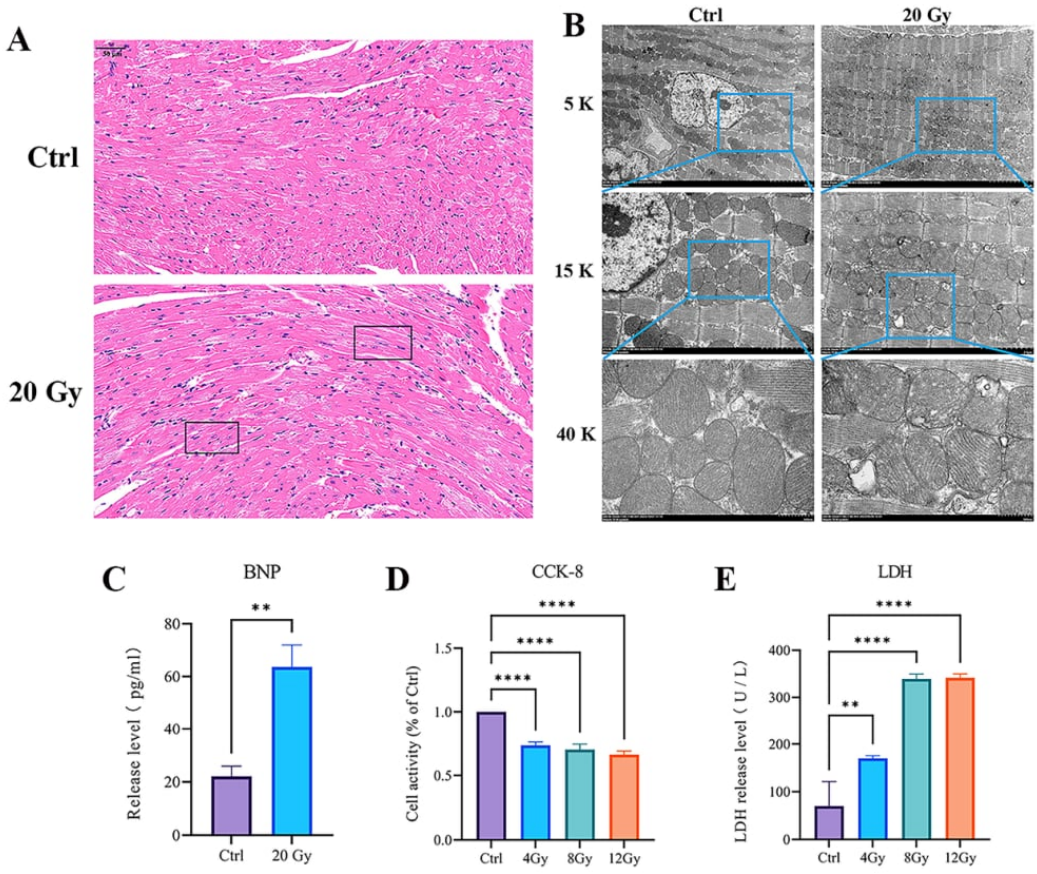

Figure 1. Myocardial tissue and H9c2 cell damage after local cardiac irradiation. (**A**,**B**) Representative images of H&E staining (scale bar, 20 μm) and TEM (scale bar, 5K-5 μm, 15K-2 μm, 40K-0.5 μm) of mouse myocardium in the control group and 12 weeks after cardiac-region irradiation at a nominal dose of 20 Gy; boxes mark the regions of interest or the areas enlarged; (**C**) Serum BNP levels in the independent validation animals; (**D**,**E**) CCK-8 relative viability and supernatant LDH levels in H9c2 cells 48 h after 4, 8, or 12 Gy irradiation. Statistical brackets indicate the comparison of each irradiation group with the control group. ** $p < 0.01$, **** $p < 0.0001$.

In the in vivo experiments, serum BNP levels were higher in the radiation group than in the control group ($p < 0.01$; Figure 1C). In H9c2 cells, viability after 4, 8, and 12 Gy was lower than in controls, and LDH release was higher than in controls in all three groups (Figure 1D,E). These results showed that X-ray irradiation produced myocardial tissue and ultrastructural damage accompanied by elevated BNP levels; the cell model likewise showed reduced viability and increased LDH release.

3.2. Overview of the Omics Data and Cross-Omics Candidate Screening

For the six WGBS samples, post-trimming data volume ranged from 81.15 to 87.30 Gb, Q30 from 91.13% to 93.81%, alignment rate from 95.31% to 95.99%, and bisulfite conversion rate from 99.3682% to 99.5908% (WGBS_QC worksheet of Supplementary Table S1). The nominal differential DMC set contained 151,522 sites, of which 850 had qvalue < 0.05. Screening of 200,618 candidate regions yielded 14,270 DMRs, comprising 4934 hypermethylated and 9336 hypomethylated regions; 34 of these reached metilene q value < 0.05. The final DMR set contained 88,179 MergedCG, and the region length accumulated as end − start + 1 was 4,533,904 bp. Of the regions, 8124 carried at least one of the listed functional annotations and 6146 received no annotation in these fields; information on all regions is given in Supplementary Table S1.

The original RNA differential set contained 341 genes, of which 216 reached BH-FDR < 0.05. The unfiltered protein quantification matrix contained 5387 rows corresponding to 5338 unique non-missing genes; the original differential screen yielded 238 rows, of which 232 had non-missing gene names. The protein ORA used the 71 unique genes meeting its effect-size criteria as the foreground. In the vendor's original differential model, only Cd200 reached BH-FDR < 0.05, but its log2FC was approximately -0.255, and it was therefore not included in the ORA foreground. A summary of the main results is given in the Results_overview worksheet of Supplementary Table S1; the full-background reanalysis is described in Sections 3.3–3.5.

Among the 34 q-value-supported DMRs, 17 were hypermethylated and 17 hypomethylated; 21 carried promoter or genebody annotations, involving 28 unique genes in total. Only Mcts2 overlapped with the RNA differential set: methylation was increased in its promoter region (methyl_diff = +0.145) while its RNA was downregulated (log2FC = −0.654, $p = 0.0475$, BH-FDR = 0.205). None of these annotated genes entered the RNA–protein intersection or the methylation–RNA gene set, and PHLDA3 was not among them either. Region annotations and overlap results are given in the FDR_supported_DMR worksheet of Supplementary Table S1.

The methylation–RNA set contained 16 region-gene associations corresponding to 14 unique genes, of which one region was of the CG type, one of the CHG type, and 14 of the CHH type. Region widths ranged from 59 to 193 bp, with 5 to 24 methylated sites per region. Seven of the 16 associations (43.8%) changed in opposite directions, with a one-sided exact binomial test giving $p = 0.7728$; the remaining associations changed in the same direction (Supplementary Figure S1A). Because one gene can correspond to several regions, the binomial test serves only as a supporting description. Among these predominantly non-CG region records, 1 of 16 overlapped physically with a retained CpG DMR, whose q value was 1.0. Complete records are given in Supplementary Table S1.

The previous study reported 39 RNA–protein overlapping molecules, of which 37 showed the same direction of change in the two layers. The present study reuses this overlapping set, tests the association between the directions of change in the two layers, and uses the set for the subsequent three-layer candidate screening [10]. A one-sided Fisher exact test was then used to assess the association of direction within the intersection ($p = 6.10 \times 10^{-5}$). A supporting binomial test against a reference probability of 0.5 for concordant direction gave $p = 1.42 \times 10^{-9}$. This concordance rate describes the selected intersection and does not represent the overall coupling between the complete transcriptome and proteome; the size of the intersection, the direction relationships, and the gene-level results are shown in Figure 2A,B and Supplementary Table S1.

PHLDA3 was the only gene overlapping all three layers, at the intersection of the methylation–RNA set and the RNA–protein set. In the original statistics, its RNA log2FC was +0.710 ($p = 0.00841$, BH-FDR = 0.0688) and its protein log2FC was approximately +0.632 ($p = 0.000517$, BH-FDR = 0.072891). The two CHH regions corresponding to Phlda3 had methylation differences of approximately +0.111 and −0.106, in opposite directions, whereas the RNA was upregulated (Supplementary Figure S1A). Neither region overlapped with a retained CpG DMR, and the joint table does not provide a regional methylation q value for them; region-level results and the full set of CpG DMRs are reported separately. The full-background expression results for PHLDA3 are given in Section 3.4.

Under the rule prioritizing three-layer overlap, PHLDA3 was listed as the primary candidate molecule. Pigt, Abcd1, Fbxw9, Celsr2, Scamp2, Parp3, Bax, Rhbdd2, and Ncdn were ranked mainly by ME2 network centrality and listed as secondary candidate molecules. The ranking reflects the pre-specified evidence rules and weights, and the association of ME2 with irradiation was nominally significant; statistical significance was not compared

among candidate molecules. The ranking is shown in Figure 2C and in the Candidates worksheet of Supplementary Table S1; the score components are given in Supplementary Table S1.

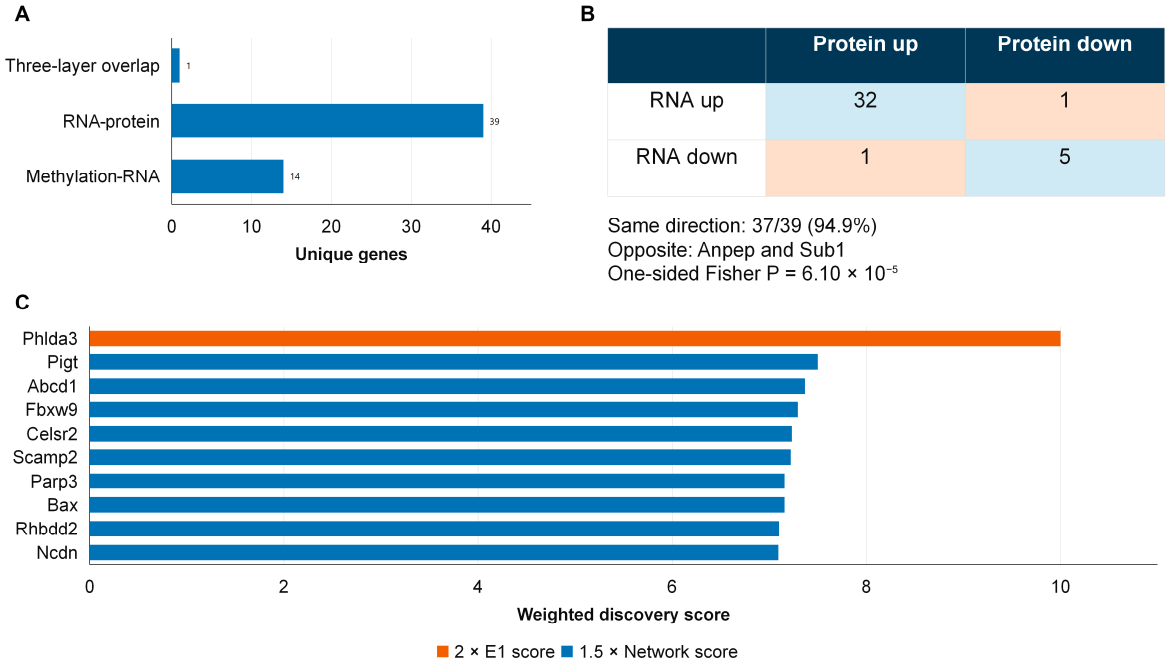

Figure 2. Cross-omics candidate screening and prioritization. (**A**) The methylation0RNA and RNA–protein sets, with PHLDA3 the only gene overlapping all three layers; (**B**) Contingency table of the direction of RNA and protein up- and downregulation, analyzed with a one-sided Fisher exact test; (**C**) Discovery-stage scores of the locked candidates, with 2 × E1 in orange and 1.5× the network score in blue; subsequent validation does not enter the score.

Merging the 20 RNA samples yielded eight non-grey co-expression modules together with the grey unassigned set ME0. In the module-trait analysis, ME2 correlated with irradiation at 0.537 ($p = 0.0146$) and ME3 at 0.499 ($p = 0.0252$), neither of which passed Bonferroni correction across the nine comparisons. ME7 was highly correlated with data source ($r = -0.992$, $p = 1.51 \times 10^{-17}$). The in-house samples were collected 12 weeks after irradiation while GSE255063 includes samples from 1 day and 6 weeks, so heterogeneity in source and time point remains visible in the merged network. The module-trait correlation matrix is shown in Supplementary Figure S1B; gene assignments and the hub gene lists are given in Supplementary Table S1.

In the DIABLO model fitted to the six fully matched animals, the correlation coefficients of the latent variables for RNA–protein, RNA–methylation, and protein–methylation in the first component were 0.9978, 0.9997, and 0.9974, respectively (Supplementary Table S1). These correlations come from the supervised fit on the training samples and describe only the latent variable relationships within the model; they are not results for classification performance or independent validation and do not contribute to candidate ranking. The correlation matrix and loadings are given in Supplementary Table S1.

3.3. Cross-Omics Functional Background and Transcriptional Response

To describe the overall cross-layer variation beyond the selected intersection, the Spearman correlation of the between-group log2FC was 0.2391 across the 5033 genes common to RNA and protein, and 57.14% changed in the same direction (Supplementary Figure S2A). Of 576 Reactome pathways testable in both layers, 160 received two-layer GSEA FDR sup-

port from RNA and the eight-sample proteome, of which 48 were in the same direction and 112 in opposite directions. The overall effect correlation between the eight-sample and the shared six-sample protein models was 0.9142, and the subset effects were close to the main model overall (Supplementary Figure S2B, Supplementary Table S2).

Among the representative pathways, aerobic respiration and electron transport (R-MMU-1428517) had NES values of −3.5853 in RNA and −3.1374 in the eight-sample proteome, mitochondrial translation (R-MMU-5368287) gave −3.3431 and −2.9281, and extracellular matrix organization (R-MMU-1474244) gave +2.3836 and +1.7460, all reaching FDR < 0.05 within their respective complete GSEA families (Figure 3A). The six-sample protein model retained the same directions and GSEA support, and collagen formation was also enriched in the positive direction. CAMERA with a fixed correlation supported some of the concordant pathways; when the within-pathway correlation was estimated, no pathway retained two-layer FDR < 0.05. Complete results are given in Supplementary Table S2.

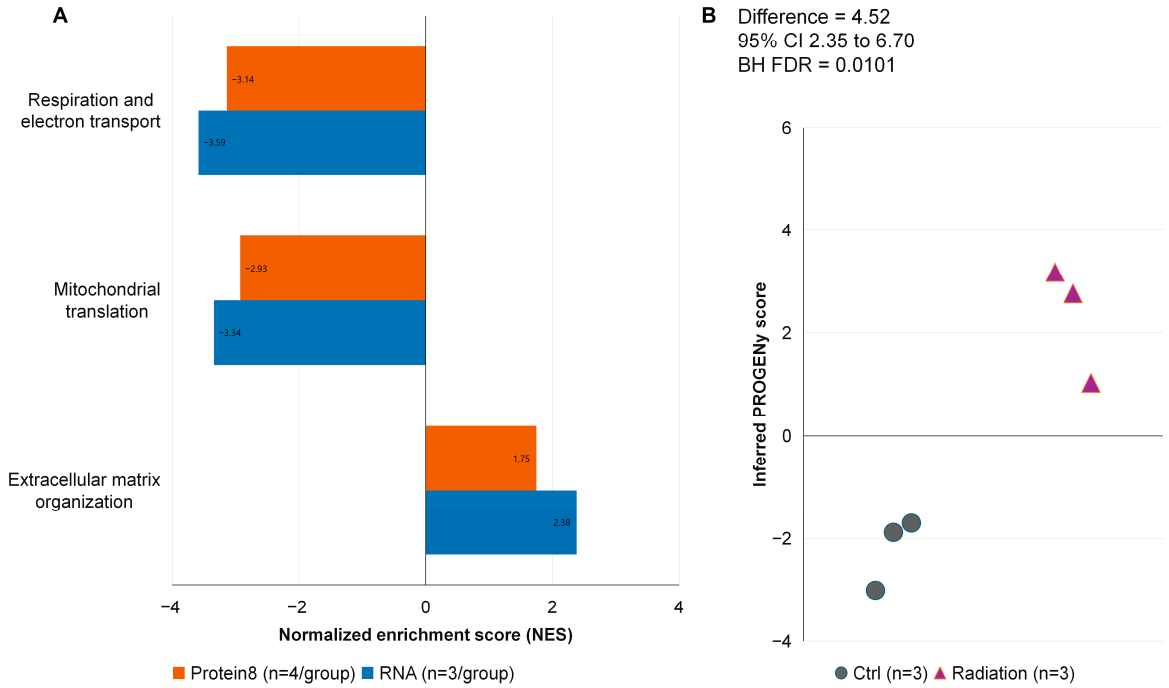

Figure 3. Mitochondrial and ECM expression programs and inference of the TGFβ transcriptional response. (**A**) NES values for representative pathways in the RNA and eight-sample protein models, with RNA in blue and protein in orange; FDR correction was applied within the complete Reactome test family for each model; (**B**) PROGENy TGFβ scores for the six animals, with the between-group difference, the 95% CI, and the FDR for the complete family; gray circles are Ctrl and purple triangles are Radiation.

The RNA/P8 common leading-edge genes numbered 92, 53, 26, and 12 for respiration/electron transport, mitochondrial translation, ECM organization, and collagen formation, respectively, of which 70, 48, 23, and 11 also entered the six-sample protein core set. All 12 common core genes for collagen formation were contained within the 26 common core genes for ECM organization. Phlda3 did not enter the leading-edge sets of these four pathways; representative members are shown in Supplementary Figure S2C,D. P8 and P6 are the main model and the shared-animal subset model of the same proteome and are not treated as two independent omics layers.

Of the 14 transcriptional responses in the main PROGENy analysis, 4 reached FDR < 0.05. The RNA-based PROGENy score for the inferred TGFβ transcriptional re-

sponse was higher in irradiated mice than in controls (between-group difference = +4.5245, 95% CI 2.3491–6.7000, BH-FDR = 0.0101301, Figure 3B). The score remained higher in irradiated mice when the top100 signature was used (BH-FDR = 0.0114841). EGFR was supported in the positive direction under both signatures, whereas NF-κB and Hypoxia were sensitive to the signature setting. The main CollecTRI analysis tested 552 factors, of which 17 had increased inferred scores reaching FDR < 0.05, their FDR values approaching 0.05. After removing Phlda3 expression and the corresponding prior edges, the same 17 factors and 4 pathways retained FDR support; p53 and PI3K did not obtain stable corrected significance. Complete scores and sensitivity results are given in Supplementary Table S3.

As a supplementary description at the discovery stage, RNA GSEA showed FDR support for processes including immune response, antigen processing and presentation, and interferon response. Of the 71 foreground genes and 5338 background genes in the protein GO biological process ORA, 69 and 5123, respectively, fell within the GO annotation range. At the protein layer, 361 terms reached $p < 0.05$, of which 175 reached BH-FDR < 0.05, the smallest BH-FDR being approximately 2.12×10^{-7}. After matching by GO identifier, 244 terms reached $p < 0.05$ in both layers and 111 reached BH-FDR < 0.05 in both layers, including processes related to interferon-β response, defense against virus, and immune cell activation.

In the discovery-stage KEGG analysis, 14 pathways were nominally significant consensus pathways across the two layers, of which 9 received two-layer BH-FDR support. In the Reactome analysis, 13 pathways were nominally significant consensus pathways across the two layers, of which only extracellular matrix organization reached two-layer BH-FDR < 0.05. Complete results for the representative GO terms and for all KEGG and Reactome pathways with two-layer FDR support are given in Supplementary Table S2. Because the protein ORA includes both up- and downregulated molecules, these consensus results reflect enrichment themes and do not indicate whether a pathway was activated or inhibited.

Separately, in the same batch of RNA samples, ssGSEA evaluated 8013 GO gene sets, of which 1718 reached nominal $p < 0.05$ but none passed BH-FDR correction (Supplementary Table S2). The nominal ssGSEA findings were therefore treated as exploratory.

3.4. PHLDA3 Expression in the In-House and Public Data

In the full expression background reanalysis performed after the candidates were locked, the RNA count model gave a PHLDA3 log2FC of +0.7058 ($p = 0.0058720$, BH-FDR = 0.0713022); the main eight-sample protein model gave +0.6318 ($p = 5.55 \times 10^{-5}$, FDR = 0.0358374), and the shared six-sample model gave +0.7479 ($p = 7.90 \times 10^{-6}$, FDR = 0.0068241). All three models showed upregulation, with FDR support obtained for both protein models while the RNA result did not reach statistical significance after BH correction. The expression distribution in the in-house animals is shown in Figure 4A,B; the original source statistics and the full-background model results are listed separately in Supplementary Table S1.

At 1 day after irradiation, the mean normalized count of Phlda3 rose from 157.3 in the control group to 1042.6 in the radiation group, with a log2FC of +2.728 ($p = 3.66 \times 10^{-13}$, BH-FDR = 2.28×10^{-9}). At 6 weeks, the mean rose from 564.7 to 1346.5, with a log2FC of +1.253 ($p = 0.0568$, BH-FDR = 0.556). The 1-day and 6-week estimates in GSE255063 were in the same direction as the change observed in the in-house 12-week RNA-seq data. In GSE255063, only the 1-day result remained significant after multiple-testing correction. Since GSE255063 had already contributed to WGCNA construction, we reused it to check the direction of *Phlda3* expression changes after candidate selection. The different irradiation protocols and sampling times limit this comparison to consistency in the direction of change

across studies. The sample expression distributions and complete statistics are shown in Figure 4C,D and Supplementary Table S1.

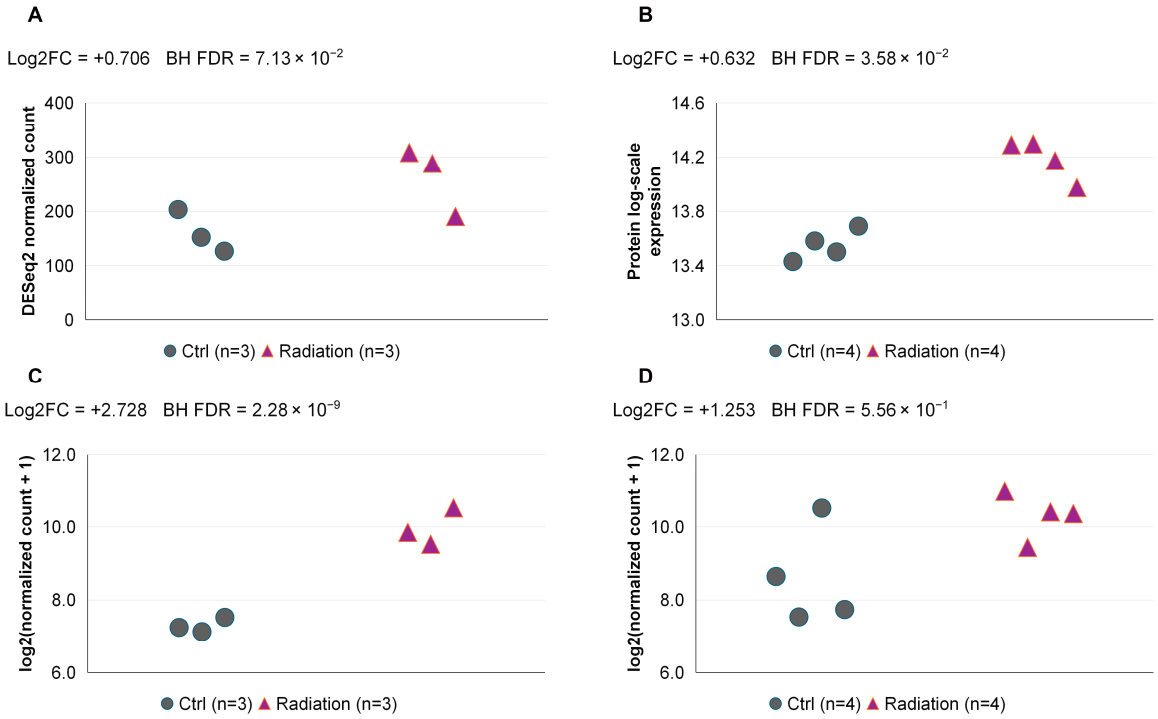

Figure 4. PHLDA3 expression in the in-house samples and in GSE255063. (**A**) DESeq2-normalized RNA counts and (**B**) log-scale protein expression in myocardial samples from the in-house cohorts. Samples in both panels were collected 12 weeks after irradiation or the corresponding control procedure; (**C**,**D**) log2(DESeq2 normalized count + 1) at 1 day and 6 weeks after irradiation in GSE255063. Each point represents one animal, with 3 animals per group in (**A**,**C**) and 4 per group in (**B**,**D**); gray circles are Ctrl and purple triangles are Radiation. The log2FC and BH-FDR are taken from the respective complete models. GSE255063 contributed to WGCNA construction and was reused here to check the direction of *Phlda3* expression changes.

3.5. Sensitivity of PHLDA3 Expression and of Same-Animal Associations

To test the dependence of the PHLDA3 expression results on individual animals, in the six RNA leave-one-out refits, the PHLDA3 effect was positive in every case, with log2FC values ranging from 0.5609 to 0.9081; 5 of 6 reached nominal $p < 0.05$ and 1 of 6 reached FDR < 0.05. The estimated PHLDA3 effects were also positive in all eight leave-one-animal-out protein models, although only one met the FDR < 0.05 threshold. These results show that the direction of upregulation was maintained while the corrected significance was sensitive to the animal composition; the full-sample model remains the main result (Supplementary Figure S3A,B, Supplementary Table S1).

Expression associations between RNA and protein were then analyzed in the six shared animals; for the 5033 genes, neither the overall nor the group-adjusted test yielded any result at FDR < 0.05. The overall Spearman correlation for PHLDA3 was 0.6000 (exact $p = 0.2416667$, FDR = 0.6613966); the group-adjusted rank-residual correlation was 0, with the group-conditioned exact p and FDR both equal to 1. After leave-one-out analysis, the adjusted correlation ranged from −0.6 to +0.6, appearing three times in each direction (Supplementary Figure S3C,D; leave-one-out results are given in Supplementary Table S1).

3.6. Expression Validation of PHLDA3 in Irradiated Myocardial Tissue

To validate the PHLDA3 expression changes indicated by the omics analysis, PHLDA3 protein expression in myocardial tissue was examined by IHC in mice from a batch independent of the omics batch. At 12 weeks after irradiation, PHLDA3 immunostaining was stronger in the irradiated myocardium than in controls, and quantitative analysis of the immunostaining showed a significant increase in the staining signal (Figure 5A,B). Because cell type-specific co-localization analysis was not performed, it cannot yet be determined whether the enhanced signal arises mainly from cardiomyocytes, fibroblasts, endothelial cells, or other cell populations.

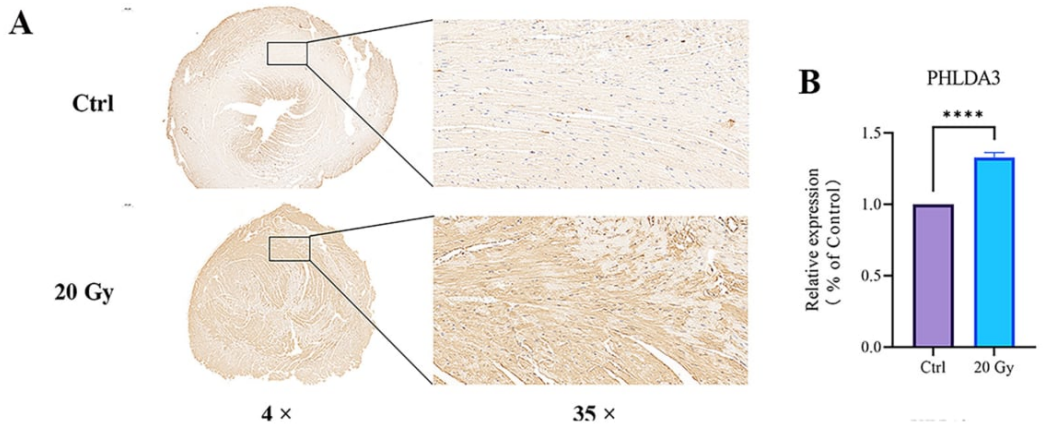

Figure 5. Validation of PHLDA3 expression in an independent animal batch. (**A**,**B**) Representative images and quantification of PHLDA3 immunohistochemistry in mouse myocardium from the control group and 12 weeks after cardiac-region irradiation at a nominal dose of 20 Gy. Scale bar, 4×-200 μm, 35×-50 μm. n = 6 mice per group. The irradiation group was compared with the control group. **** $p < 0.0001$.

4. Discussion

This study integrated DNA methylation, RNA, and protein information, identified PHLDA3 as the only three-layer overlapping candidate molecule, and characterized its expression through full-background analysis and sample-sensitivity checks. IHC in myocardial tissue from an independent cohort of mice further supported increased PHLDA3 expression after irradiation. Omics-based screening, checking of a dataset from a public database, and expression assays in tissue thus formed mutually complementary evidence, but they answer different questions and rest on different statistical backgrounds.

Methylation changes varied by region [8], and the two CHH regions annotated to *Phlda3* showed changes in opposite directions. The available data do not yet establish whether the methylation changes at these two CHH regions are correlated with Phlda3 expression at the individual-animal level. Establishing a direct regulatory relationship would additionally require validating the regional methylation changes in independent samples and testing whether altering the methylation state of the relevant regions affects Phlda3 expression. These records are predominantly non-CG regions and cannot be fitted directly to a single interpretation linking promoter CpG methylation to transcriptional repression. The q value-supported CpG DMRs and the joint records above present results at different levels, and their annotated genes did not converge on PHLDA3. Regional changes, three-layer molecular overlap, and the direction of expression should therefore be interpreted as separate evidence layers.

The high RNA–protein concordance within the selected intersection was less pronounced across all shared genes [9]. PHLDA3 RNA and protein both increased after irradi-

ation, with no evidence of an association between their levels across individual animals after adjustment for group.

Preranked GSEA showed negative enrichment of mitochondrial gene sets and positive enrichment of extracellular matrix organization gene sets in both the transcriptomic and proteomic analyses; the discovery-stage RNA GSEA and protein ORA pointed instead to immune- and matrix-related themes [31]. Previous studies of local cardiac irradiation in mice have also reported mitochondrial damage and abnormal energy metabolism [32,33], and other mouse irradiation studies have reported TGF-β1/Smad-related expression changes and myocardial fibrosis [34]. The changes in mitochondrial expression programs and the mitochondrial ultrastructural damage seen by TEM therefore form complementary evidence at the morphological and molecular levels. The higher PROGENy score reflects a TGFβ-related transcriptional response inferred from RNA expression. TGFβ pathway activity was not directly measured. The inferred TGFβ response provides supporting information for the matrix-related theme within the same transcriptome [35]. CAMERA with estimated gene correlation retained no two-layer significance, indicating that the enrichment results are sensitive to the correlation structure; Phlda3 also did not enter the leading-edge sets of the representative pathways, so these expression programs cannot be designated as its downstream mechanisms.

The merged WGCNA was used to extend the network input at the discovery stage, and the public-data expression analysis was used to check the direction of change in the candidate molecules that had been locked. The associations of ME2 and ME3 with irradiation were only nominally significant, and ME7 was highly correlated with study source, indicating that the merged network remains affected by differences in source and time point. In GSE255063, Phlda3 was significantly upregulated at 1 day and retained the same direction of change at 6 weeks without reaching significance, providing directional support across time points together with the in-house 12-week result. Because this dataset had already contributed to the network construction, this check does not serve as independent external validation of the entire discovery workflow, nor did it feed back into the candidate scores. The source study of GSE255063 reported inflammatory cell infiltration in the myocardium 1 day after irradiation and an increase in hypertrophic cardiomyocytes with myocardial fibrosis at 6 weeks. In the present analysis of this dataset, the upregulation of Phlda3 at 1 day may accompany an early myocardial stress response. Enhanced myocardial PHLDA3 immunostaining was also observed at 12 weeks after irradiation in the present study, which indicates the need to examine further the relation of PHLDA3 to later-stage myocardial injury and tissue remodeling. Because the irradiation conditions differed between the two studies and the present study sampled only at 12 weeks, the current results cannot establish the temporal pattern of PHLDA3 expression, nor determine whether PHLDA3 has different functions in the early and later stages of injury.

The established links of PHLDA3 with p53 regulation and Akt signaling inhibition provide biological clues for understanding its response to irradiation [36,37]. In our previous study, X-ray irradiation reduced the ratio of phosphorylated to total Akt in H9c2 cells [10]. In myocardial hypoxia/reoxygenation models, PHLDA3 intervention has been associated with endoplasmic reticulum stress-related apoptosis and changes in PI3K/AKT signaling [38]; ischemia/reperfusion studies have also reported a relationship between PHLDA3 and ferroptosis of cardiomyocytes [39,40]. These findings provide the myocardial stress context, but the type of injury differs from that of the present study, and the same mechanism cannot be extrapolated to RIHD on this basis. The present study did not measure the functional activity of p53 or Akt, and p53 and PI3K in the transcriptional response inference did not obtain stable corrected significance either; the available results cannot establish that these signals mediate PHLDA3 changes. Based on the previously reported link

between PHLDA3 and Akt signaling, we hypothesize that increased PHLDA3 expression after irradiation may influence the myocardial injury response by modulating Akt activity. This hypothesis could be tested by altering PHLDA3 expression and assessing both Akt activity and the severity of injury after irradiation. The interferon and antiviral themes in RNA can also be linked to the existing model in which micronuclei form after DNA damage and elicit cGAS/STING responses [41,42]; the cytosolic DNA-sensing pathway obtained BH-FDR support at the RNA layer but did not reach nominal significance at the protein layer. Because micronuclei, cytosolic DNA, and the relevant phosphorylation events were not measured directly, this interpretation remains a biological hypothesis.

Extracellular vesicles (EVs) may participate in the transmission of intercellular stress signals after irradiation. Rosa et al. proposed in a review of brachytherapy that differences in local dose may affect EV-mediated intercellular communication [43]. Luo et al. reported in an in vitro study that EVs released by irradiated human placenta-derived mesenchymal stem cells increased apoptosis and DNA damage in H9c2 cells [44]. These observations provide a lead for investigating the role of EVs in radiation-induced myocardial injury. EVs were not examined in the present study, so whether they contribute to myocardial injury in this model, or whether they are related to the changes in PHLDA3 expression, remains to be established.

We used a mouse model of RIHD to examine myocardial injury and radiation-associated molecular alterations 12 weeks after a single nominal 20 Gy X-ray exposure directed at the cardiac region. Because the actual absorbed dose to the heart and the extent of cardiac coverage could not be verified, the myocardial findings should be interpreted in the context of the irradiation setup described in Section 2.1. In clinical practice, thoracic radiotherapy is usually delivered in fractions, and the radiation dose and extent delivered to the heart vary with the tumour position and the treatment plan. The intervals between fractions also allow time for tissue repair, so whether the present results can be reproduced under clinically relevant fractionated irradiation remains to be verified. A lead shield with 1-cm apertures was used to limit exposure of tissues surrounding the cardiac region. Lung dose and irradiated lung volume were not quantified, and lung histopathology data were unavailable. The extent of incidental pulmonary exposure and its potential contribution to the myocardial changes observed at 12 weeks therefore remain uncertain. The omics and histopathological analyses were based on mice that survived to the scheduled 12-week endpoint. Deaths in the irradiated groups may have introduced survivorship bias by affecting which animals were available for analysis. The direction and magnitude of any resulting bias remain uncertain. The in vitro experiments used the rat-derived H9c2 cell line and assessed cell viability and LDH release 48 h after irradiation. This model is suitable for evaluating short-term cellular injury responses, but it does not fully reproduce the characteristics of mature human cardiomyocytes or the interactions among the different cell types in intact myocardial tissue. The PHLDA3 expression changes observed here may therefore provide a candidate lead for subsequent studies, and their relevance to human radiation-related myocardial injury remains to be determined. The present study primarily evaluated myocardial structure and molecular changes after irradiation and did not directly measure cardiac function; it therefore remains to be determined whether these changes were accompanied by cardiac dysfunction. Only male mice were included in this study. Sex-related differences in myocardial transcriptional responses and cardiac phenotypes have been reported in BALB/cJ mice after cardiac irradiation [45]. Whether female mice would exhibit a similar increase in myocardial PHLDA3 expression or comparable changes across the three omics layers under the same experimental conditions remains unknown.

The omics sample size in this study is limited. WGBS and RNA-seq included three mice per group, the main proteome analysis included four per group, and the three-layer

paired analysis was based on the six shared mice. The small number of biological replicates limits the precision of between-group effect estimates and may also reduce the power to detect small-to-moderate differences after correction for multiple testing. Because cross-omics candidate screening relies on the intersection of the differential sets from each layer, individual variation may determine whether molecules close to the screening threshold are included, and may thus change the candidate set and its priority order. For PHLDA3, both the RNA and the protein retained the direction of upregulation in the leave-one-out analyses, but the corrected significance varied with the composition of the samples. The reproducibility of the other candidate molecules and of the cross-omics screening results remains to be tested in larger independent omics samples.

5. Conclusions

The three-layer integration identified PHLDA3 as the only gene shared by the methylation–RNA and RNA–protein sets and prioritized it for further study in this mouse model of RIHD. Its RNA and protein were upregulated in the same direction, with the full-background protein model obtaining FDR support; the RNA did not pass FDR correction over the full gene background, but the direction of upregulation was maintained in the leave-one-out analyses and in the expression check in GSE255063. IHC in an independent animal batch further supports the increase in PHLDA3 protein expression after irradiation. Pathway analyses showed negative enrichment of mitochondrial gene sets, positive enrichment of extracellular matrix organization gene sets, and a higher inferred TGFβ transcriptional response score after irradiation. The functional contribution of PHLDA3 to radiation-induced myocardial injury and the role of DNA methylation in regulating its expression remain unclear. Its potential as a therapeutic target depends on whether modulating PHLDA3 can alleviate myocardial injury after irradiation, which remains to be tested experimentally.

Supplementary Materials: The following supporting information can be downloaded at: https://www.mdpi.com/article/10.3390/biology15232192/s1, Supplementary Figure S1: Methylation-RNA direction and WGCNA module associations; Supplementary Figure S2: Full-background effects and common core members of pathways; Supplementary Figure S3: PHLDA3 leave-one-out sensitivity and same-animal RNA-protein associations; Supplementary Table S1: DNA methylation, cross-omics integration, and PHLDA3 analyses; Supplementary Table S2: Differential expression and pathway enrichment results; Supplementary Table S3: Inferred transcription factor and pathway activities; Supplementary Methods S1: Omics preprocessing, differential analysis, and gene identifier handling; Methods S2: Merged co-expression network; Methods S3: Cross-layer direction, candidate ranking, and DIABLO; Methods S4: Enrichment backgrounds and pathway statistics; Methods S5: Transcriptional response and transcription factor inference; Methods S6: Targeted expression check in GSE255063; Methods S7: Sensitivity and leave-one-out analyses; Methods S8: Same-animal associations and exact tests.

Author Contributions: G.W.: Writing—original draft, Writing—review & editing. Y.Z.: Data curation, Formal analysis. A.-J.W.: Data curation, Methodology, Software. P.X.: Funding acquisition, Project administration. All authors have read and agreed to the published version of the manuscript.

Funding: This work was supported by grants from the National Natural Science Foundation of China (No. 82460051), the Natural Science Foundation of Gansu Province (Grant No. 25JRRA286).

Institutional Review Board Statement: All procedures were approved by the Ethics Committee of Gansu Provincial Hospital and complied with national animal care guidelines. The experiments were performed under a project license (approval No. 2024-341; date of approval:04-25-2024) granted by the ethics board of Gansu Provincial Hospital in compliance with national guidelines for the care and use of animals.

Data Availability Statement: The WGBS raw sequence data reported in this paper have been deposited in the Genome Sequence Archive in National Genomics Data Center, China National Center for Bioinformation / Beijing Institute of Genomics, Chinese Academy of Sciences (GSA: CRA043688) and are publicly accessible at https://ngdc.cncb.ac.cn/gsa/s/WzZsTklq(accessed on 2 November 2026). Except for WGBS data, other data can be provided upon reasonable request by contacting the corresponding author. The public transcriptome data used in this study were obtained from the NCBI Gene Expression Omnibus (GEO) database under accession number GSE255063. The dataset was used for the merged co-expression network analysis and for checking the direction of Phlda3 expression changes. The processed gene count matrix is publicly available from the GEO record, and the raw sequencing data can be obtained through its associated SRA record. Supplementary Table S1 provides differential methylation results, cross-omics screening results, candidate rankings, and PHLDA3 sensitivity analyses. Supplementary Table S2 provides gene-level differential expression statistics for RNA and protein and the pathway enrichment results. Supplementary Table S3 provides the input data used for transcriptional response inference, the inferred response scores, and the corresponding statistical and sensitivity analyses. The Supplementary Methods describe the analysis procedures and parameters.

Conflicts of Interest: The authors declare no conflicts of interest.

References

1. Zhao, C.; Xu, S.; Yang, Y.; Shen, X.; Wang, J.; Xing, S.; Yu, Z. Intersection of Cardio-Oncology: An Overview of Radiation-Induced Heart Disease in the Context of Tumors. *J. Am. Heart Assoc.* **2025**, *14*, e040937. [CrossRef] [PubMed]
2. Wang, H.; Wei, J.; Zheng, Q.; Meng, L.; Xin, Y.; Yin, X.; Jiang, X. Radiation-induced heart disease: A review of classification, mechanism and prevention. *Int. J. Biol. Sci.* **2019**, *15*, 2128–2138. [CrossRef] [PubMed]
3. van Nimwegen, F.A.; Schaapveld, M.; Janus, C.P.; Krol, A.D.; Petersen, E.J.; Raemaekers, J.M.; Kok, W.E.; Aleman, B.M.; van Leeuwen, F.E. Cardiovascular disease after Hodgkin lymphoma treatment: 40-year disease risk. *JAMA Intern. Med.* **2015**, *175*, 1007–1017. [CrossRef] [PubMed]
4. Saiki, H.; Moulay, G.; Guenzel, A.J.; Liu, W.; Decklever, T.D.; Classic, K.L.; Pham, L.; Chen, H.H.; Burnett, J.C.; Russell, S.J.; et al. Experimental cardiac radiation exposure induces ventricular diastolic dysfunction with preserved ejection fraction. *Am. J. Physiol. Heart Circ. Physiol.* **2017**, *313*, H392–H407. [CrossRef] [PubMed]
5. Darby, S.C.; Ewertz, M.; McGale, P.; Bennet, A.M.; Blom-Goldman, U.; Brønnum, D.; Correa, C.; Cutter, D.; Gagliardi, G.; Gigante, B.; et al. Risk of ischemic heart disease in women after radiotherapy for breast cancer. *N. Engl. J. Med.* **2013**, *368*, 987–998. [CrossRef] [PubMed]
6. Maunakea, A.K.; Nagarajan, R.P.; Bilenky, M.; Ballinger, T.J.; D'Souza, C.; Fouse, S.D.; Johnson, B.E.; Hong, C.; Nielsen, C.; Zhao, Y.; et al. Conserved role of intragenic DNA methylation in regulating alternative promoters. *Nature* **2010**, *466*, 253–257. [CrossRef] [PubMed]
7. Jovanovic, M.; Rooney, M.S.; Mertins, P.; Przybylski, D.; Chevrier, N.; Satija, R.; Rodriguez, E.H.; Fields, A.P.; Schwartz, S.; Raychowdhury, R.; et al. Immunogenetics. Dynamic profiling of the protein life cycle in response to pathogens. *Science* **2015**, *347*, 1259038. [CrossRef] [PubMed]
8. Gilsbach, R.; Preissl, S.; Grüning, B.A.; Schnick, T.; Burger, L.; Benes, V.; Würch, A.; Bönisch, U.; Günther, S.; Backofen, R.; et al. Dynamic DNA methylation orchestrates cardiomyocyte development, maturation and disease. *Nat. Commun.* **2014**, *5*, 5288. [CrossRef] [PubMed]
9. Wang, D.; Eraslan, B.; Wieland, T.; Hallström, B.; Hopf, T.; Zolg, D.P.; Zecha, J.; Asplund, A.; Li, L.H.; Meng, C.; et al. A deep proteome and transcriptome abundance atlas of 29 healthy human tissues. *Mol. Syst. Biol.* **2019**, *15*, e8503. [CrossRef] [PubMed]
10. Wang, G.; Li, Y.L.; Wang, B.W.; Wang, R.; Wang, Y.; Shu, Y.B.; Zhang, W.B.; Wu, P.; Hu, Y.J.; Lu, W.J.; et al. Targeting DNMT1 Attenuates Radiation-Induced Heart Disease: An Integrated Multiomic and Functional Study. *FASEB J.* **2026**, *40*, e71931. [CrossRef] [PubMed]
11. Park, J.; Lee, H.J.; Han, Y.K.; Kang, K.; Yi, J.M. Identification of DNA methylation biomarkers for evaluating cardiovascular disease risk from epigenome profiles altered by low-dose ionizing radiation. *Clin. Epigenet.* **2024**, *16*, 19. [CrossRef] [PubMed]
12. Bolger, A.M.; Lohse, M.; Usadel, B. Trimmomatic: A flexible trimmer for Illumina sequence data. *Bioinformatics* **2014**, *30*, 2114–2120. [CrossRef] [PubMed]
13. Xi, Y.; Li, W. BSMAP: Whole genome bisulfite sequence MAPping program. *BMC Bioinform.* **2009**, *10*, 232. [CrossRef] [PubMed]
14. Akalin, A.; Kormaksson, M.; Li, S.; Garrett-Bakelman, F.E.; Figueroa, M.E.; Melnick, A.; Mason, C.E. methylKit: A comprehensive R package for the analysis of genome-wide DNA methylation profiles. *Genome Biol.* **2012**, *13*, R87. [CrossRef] [PubMed]

15. Jühling, F.; Kretzmer, H.; Bernhart, S.H.; Otto, C.; Stadler, P.F.; Hoffmann, S. metilene: Fast and sensitive calling of differentially methylated regions from bisulfite sequencing data. *Genome Res.* **2016**, *26*, 256–262. [CrossRef] [PubMed]
16. Liu, C.; Shi, J.; Xing, L.; Yao, B.; Liu, J.; Wang, Y.; Fan, J. Discovery and confirmation of crucial genes associated with radiation-induced heart disease. *Int. J. Med. Sci.* **2025**, *22*, 1278–1291. [CrossRef] [PubMed]
17. Johnson, W.E.; Li, C.; Rabinovic, A. Adjusting batch effects in microarray expression data using empirical Bayes methods. *Biostatistics* **2007**, *8*, 118–127. [CrossRef] [PubMed]
18. Langfelder, P.; Horvath, S. WGCNA: An R package for weighted correlation network analysis. *BMC Bioinform.* **2008**, *9*, 559. [CrossRef] [PubMed]
19. Singh, A.; Shannon, C.P.; Gautier, B.; Rohart, F.; Vacher, M.; Tebbutt, S.J. KA LC: DIABLO: An integrative approach for identifying key molecular drivers from multi-omics assays. *Bioinformatics* **2019**, *35*, 3055–3062. [CrossRef] [PubMed]
20. Ashburner, M.; Ball, C.A.; Blake, J.A.; Botstein, D.; Butler, H.; Cherry, J.M.; Davis, A.P.; Dolinski, K.; Dwight, S.S.; Eppig, J.T.; et al. Gene ontology: Tool for the unification of biology. The Gene Ontology Consortium. *Nat. Genet.* **2000**, *25*, 25–29. [CrossRef] [PubMed]
21. Kanehisa, M.; Goto, S. KEGG: Kyoto encyclopedia of genes and genomes. *Nucleic Acids Res.* **2000**, *28*, 27–30. [CrossRef] [PubMed]
22. Milacic, M.; Beavers, D.; Conley, P.; Gong, C.; Gillespie, M.; Griss, J.; Haw, R.; Jassal, B.; Matthews, L.; May, B.; et al. The Reactome Pathway Knowledgebase 2024. *Nucleic Acids Res.* **2024**, *52*, D672–D678. [CrossRef] [PubMed]
23. Hänzelmann, S.; Castelo, R.; Guinney, J. GSVA: Gene set variation analysis for microarray and RNA-seq data. *BMC Bioinform.* **2013**, *14*, 7. [CrossRef] [PubMed]
24. Barbie, D.A.; Tamayo, P.; Boehm, J.S.; Kim, S.Y.; Moody, S.E.; Dunn, I.F.; Schinzel, A.C.; Sandy, P.; Meylan, E.; Scholl, C.; et al. Systematic RNA interference reveals that oncogenic KRAS-driven cancers require TBK1. *Nature* **2009**, *462*, 108–112. [CrossRef] [PubMed]
25. Subramanian, A.; Tamayo, P.; Mootha, V.K.; Mukherjee, S.; Ebert, B.L.; Gillette, M.A.; Paulovich, A.; Pomeroy, S.L.; Golub, T.R.; Lander, E.S.; et al. Gene set enrichment analysis: A knowledge-based approach for interpreting genome-wide expression profiles. *Proc. Natl. Acad. Sci. USA* **2005**, *102*, 15545–15550. [CrossRef] [PubMed]
26. Wu, D.; Smyth, G.K. Camera: A competitive gene set test accounting for inter-gene correlation. *Nucleic Acids Res.* **2012**, *40*, e133. [CrossRef] [PubMed]
27. Robinson, M.D.; Oshlack, A. A scaling normalization method for differential expression analysis of RNA-seq data. *Genome Biol.* **2010**, *11*, R25. [CrossRef] [PubMed]
28. Schubert, M.; Klinger, B.; Klünemann, M.; Sieber, A.; Uhlitz, F.; Sauer, S.; Garnett, M.J.; Blüthgen, N.; Saez-Rodriguez, J. Perturbation-response genes reveal signaling footprints in cancer gene expression. *Nat. Commun.* **2018**, *9*, 20. [CrossRef] [PubMed]
29. Müller-Dott, S.; Tsirvouli, E.; Vazquez, M.; Ramirez Flores, R.O.; Badia, I.M.P.; Fallegger, R.; Türei, D.; Lægreid, A.; Saez-Rodriguez, J. Expanding the coverage of regulons from high-confidence prior knowledge for accurate estimation of transcription factor activities. *Nucleic Acids Res.* **2023**, *51*, 10934–10949. [CrossRef] [PubMed]
30. Badia, I.M.P.; Vélez Santiago, J.; Braunger, J.; Geiss, C.; Dimitrov, D.; Müller-Dott, S.; Taus, P.; Dugourd, A.; Holland, C.H.; Ramirez Flores, R.O.; et al. decoupleR: Ensemble of computational methods to infer biological activities from omics data. *Bioinform. Adv.* **2022**, *2*, vbac016. [CrossRef] [PubMed]
31. Yan, X.; Zhao, J.; Shi, Q.; Yan, R.; Li, S.; Song, J. Immune and stromal remodeling underlies radiation-induced heart injury: Insights from single-cell transcriptomics. *Front. Cardiovasc. Med.* **2026**, *13*, 1836858. [CrossRef] [PubMed]
32. Xu, P.; Yi, Y.; Luo, Y.; Liu, Z.; Xu, Y.; Cai, J.; Zeng, Z.; Liu, A. Radiation-induced dysfunction of energy metabolism in the heart results in the fibrosis of cardiac tissues. *Mol. Med. Rep.* **2021**, *24*, 842. [CrossRef] [PubMed]
33. Barjaktarovic, Z.; Shyla, A.; Azimzadeh, O.; Schulz, S.; Haagen, J.; Dörr, W.; Sarioglu, H.; Atkinson, M.J.; Zischka, H.; Tapio, S. Ionising radiation induces persistent alterations in the cardiac mitochondrial function of C57BL/6 mice 40 weeks after local heart exposure. *Radiother. Oncol.* **2013**, *106*, 404–410. [CrossRef] [PubMed]
34. Zhang, J.; He, X.; Bai, X.; Sun, Y.; Jiang, P.; Wang, X.; Li, W.; Zhang, Y. Protective effect of trimetazidine in radiation-induced cardiac fibrosis in mice. *J. Radiat. Res.* **2020**, *61*, 657–665. [CrossRef] [PubMed]
35. Khalil, H.; Kanisicak, O.; Prasad, V.; Correll, R.N.; Fu, X.; Schips, T.; Vagnozzi, R.J.; Liu, R.; Huynh, T.; Lee, S.J.; et al. Fibroblast-specific TGF-β-Smad2/3 signaling underlies cardiac fibrosis. *J. Clin. Investig.* **2017**, *127*, 3770–3783. [CrossRef] [PubMed]
36. Kawase, T.; Ohki, R.; Shibata, T.; Tsutsumi, S.; Kamimura, N.; Inazawa, J.; Ohta, T.; Ichikawa, H.; Aburatani, H.; Tashiro, F.; et al. PH domain-only protein PHLDA3 is a p53-regulated repressor of Akt. *Cell* **2009**, *136*, 535–550. [CrossRef] [PubMed]
37. Brady, C.A.; Jiang, D.; Mello, S.S.; Johnson, T.M.; Jarvis, L.A.; Kozak, M.M.; Kenzelmann Broz, D.; Basak, S.; Park, E.J.; McLaughlin, M.E.; et al. Distinct p53 transcriptional programs dictate acute DNA-damage responses and tumor suppression. *Cell* **2011**, *145*, 571–583. [CrossRef] [PubMed]

38. Liu, K.; Chen, Y.; Ai, F.; Li, Y.Q.; Zhang, K.; Zhang, W.T. PHLDA3 inhibition attenuates endoplasmic reticulum stress-induced apoptosis in myocardial hypoxia/reoxygenation injury by activating the PI3K/AKT signaling pathway. *Exp. Ther. Med.* **2021**, *21*, 613. [CrossRef] [PubMed]
39. Zhu, L.; Zhu, Q.; Chen, Z.; Tao, Y.; Hu, J.; Wang, D.; Lin, Y.; Yang, H.; Gao, C.; Zhang, W. Estrogen mitigates ischemia-reperfusion injury by inhibiting cardiomyocyte ferroptosis through the downregulation of PHLDA3 expression. *Free Radic. Biol. Med.* **2025**, *232*, 1–14. [CrossRef] [PubMed]
40. Liu, J.; Liu, X.; Hui, X.; Cai, L.; Li, X.; Yang, Y.; Shu, S.; Wang, F.; Xia, H.; Li, S. Novel Role for Pleckstrin Homology-Like Domain Family A, Member 3 in the Regulation of Pathological Cardiac Hypertrophy. *J. Am. Heart Assoc.* **2019**, *8*, e011830. [CrossRef] [PubMed]
41. Mackenzie, K.J.; Carroll, P.; Martin, C.A.; Murina, O.; Fluteau, A.; Simpson, D.J.; Olova, N.; Sutcliffe, H.; Rainger, J.K.; Leitch, A.; et al. cGAS surveillance of micronuclei links genome instability to innate immunity. *Nature* **2017**, *548*, 461–465. [CrossRef] [PubMed]
42. Harding, S.M.; Benci, J.L.; Irianto, J.; Discher, D.E.; Minn, A.J.; Greenberg, R.A. Mitotic progression following DNA damage enables pattern recognition within micronuclei. *Nature* **2017**, *548*, 466–470. [CrossRef] [PubMed]
43. Rosa, E.; Vaccaro, M.; Fionda, B.; Lancellotta, V.; Ciasca, G.; Dragonetti, P.; Di Maio, L.; Marazzi, F.; Marampon, F.; Mangoni, M.; et al. Revisiting the Abscopal Effect in the Era of Immuno-Radiotherapy: Mechanisms, Challenges, and Clinical Perspectives. *Biomolecules* **2026**, *16*, 1185. [CrossRef] [PubMed]
44. Luo, L.; Yan, C.; Fuchi, N.; Kodama, Y.; Zhang, X.; Shinji, G.; Miura, K.; Sasaki, H.; Li, T.S. Mesenchymal stem cell-derived extracellular vesicles as probable triggers of radiation-induced heart disease. *Stem Cell Res. Ther.* **2021**, *12*, 422. [CrossRef] [PubMed]
45. Whelan, E.R.; Perona, E.E.; Fliess, J.J.; Kocsis, S.C.; Weigel, G.J.; McCabe, E.J.; Hamilton, C.; Florio, D.N.; Balamurugan, V.; Beetler, D.J.; et al. Sex differences in a mouse model of radiation-induced cardiomyopathy. *Biol. Sex Differ.* **2026**, *17*, 166. [CrossRef] [PubMed]

Disclaimer/Publisher's Note: The statements, opinions and data contained in all publications are solely those of the individual author(s) and contributor(s) and not of MDPI and/or the editor(s). MDPI and/or the editor(s) disclaim responsibility for any injury to people or property resulting from any ideas, methods, instructions or products referred to in the content.